



# Nonuniqueness of the fatigue threshold



S. Alkan, H. Sehitoglu\*

Department of Mechanical Science and Engineering, University of Illinois at Urbana-Champaign, 1206 W. Green Street, Urbana, IL 61801, USA

## ARTICLE INFO

### Article history:

Received 10 May 2017

Received in revised form 23 July 2017

Accepted 25 July 2017

Available online 26 July 2017

### Keywords:

Fatigue crack growth

Threshold stress intensity range

Nano-grained alloy

Slip irreversibility

Grain boundary-dislocation interaction

## ABSTRACT

The fatigue crack growth prediction near the threshold regime remains one of the most challenging fields in fatigue research. In previous studies, the threshold effects have been incorporated into fatigue crack growth models upon modification of the Paris Law in an empirical fashion. In this work, without a priori assumptions and empirical constants, we derived the threshold levels with a combination of molecular dynamics and continuum calculations. We illustrate that the threshold value is non-unique and depends on the state of the microstructure surrounding the crack. Also, in reality, we envisage very low fatigue crack growth rates near the 'threshold' and not a cut-off value, which is consistent with the experimental trends. In the model, the microstructure is characterized by the grain boundary types, the grain size, and the initial dislocation density. We derive friction stresses for the forward and the reverse motion of the crack tip dislocations interacting with the grain boundaries which allow determination of the irreversible crack tip displacements. We illustrate the benefits of sigma-3 grain boundaries, finer grain sizes and the shielding dislocations at the crack tip on improving the near-threshold fatigue crack growth behavior.

© 2017 Elsevier Ltd. All rights reserved.

## 1. Introduction

### 1.1. Microstructure sensitive crack growth regime

Most structures undergo low crack growth rates and operate at stress intensity levels well below that are characterized by the Paris law. Under these circumstances, denoted as the threshold growth regime, the fatigue crack propagation rate exhibits substantial variability and determination of a unique threshold stress intensity level below which the fatigue crack attains a non-propagating state is an onerous task. In the threshold regime, the Fatigue Crack Growth (FCG) rate curves are segmented and are affected by the material microstructure. The interplay between the advancing crack and the surrounding microstructure stands out as a challenging problem in predicting metal fatigue life. To that end, there is a strong need for incorporating the near threshold FCG behavior in a model for estimation of the metal fatigue life or correctly deciding the inspection intervals within a damage tolerance approach. Unless there is a description that encompasses the threshold region, the predictive capabilities have significant shortcomings.

In this study, we address the fatigue threshold determination which remains one of the unsolved topics in the mechanics of fatigue. The fatigue threshold level is difficult to determine exper-

imentally and its continuum scale treatment as an empirical constant is not sufficient. In fact, experimental methods of measuring thresholds have been under considerable debate. Currently suggested methods described within ASTM E 647-15 standard [1], besides lacking a scientific explanation for the loading history effects, do not address the role of non-continuum effects on the threshold determination. Our calculations of the threshold without using empirical constants underscores the need to incorporate the microstructural parameters in an atomistic-continuum framework. To characterize the non-uniqueness, this paper underscores the confluence of three main variables surrounding the crack front: the grain boundary type, the shielding dislocations, and the grain dimension.

Within the last three decades, nanograins were introduced into the engineering materials to impart superior mechanical properties such as ultrahigh yield and fracture strengths on the order of GPa's as well as high wear resistance. [2,3]. Unfortunately, many nanograined alloys exhibit low ductility despite high strength. A major advancement for the superior ductility in nanograined materials occurred with the introduction of nanotwins via electrodeposition and deformation processing [4–6]. The nanotwinned microstructures promote glide motion along the twin lamellae and incorporate dislocations at the interfaces acting as efficient slip barriers [3,7,8]. Furthermore, the FCG resistance of alloys can be improved with nanosized grains and twins compared to a coarse grained microstructure [9–12]. The improved fatigue crack impedance in this class of materials originates from the interaction

\* Corresponding author.

E-mail address: [huseyin@illinois.edu](mailto:huseyin@illinois.edu) (H. Sehitoglu).

of the crack tip emitted dislocations with the grain and twin boundaries [13–15]. Admittedly, a comprehensive understanding of the slip transmission mechanisms across a grain/twin boundary is necessary to shed light on the microstructural parameters promoting the FCG resistance of the nanostructured materials. Contemporary characterization and modelling tools allow us to decipher the prevailing mechanisms at different scales—from short range atomistic interactions to long range continuum scale behavior. In this study, utilizing (i) Electron Backscatter Diffraction (EBSD) analyses for the microstructure characterization, (ii) Molecular Dynamics (MD) simulations for the atomistic scale identification of slip transfer mechanisms across different types of grain and twin boundaries and finally (iii) continuum scale dislocation motion simulations for the macroscopic FCG modelling, we will present a multiscale analysis on the FCG behavior of nanocrystalline Ni-2.89 wt.% Co alloy, denoted as Ni-Co herein after, manufactured by the electrodeposition technique [16].

In the near threshold FCG regime (also known as Stage I) that we will focus on, the microstructural features such as grain and twin boundaries can obstruct the glide motion of the crack tip emitted dislocations along the activated crystal slip system [14,17,18]. This microstructure sensitive crack growth mechanism is illustrated in Fig. 1 below. As can be seen, the obstruction of the dislocation motion during forward and reverse portions of the cyclic loading introduces irreversible displacements at the crack tip promoting the crack growth. The residual slip vectors resulting from the slip transmission across the boundaries during cyclic dislocation glide, (i.e.  $b_{r,forward}$  and  $b_{r,reverse}$ ), are of paramount importance in crack growth as the combination of these vectors directly quantify the irreversible cyclic crack tip advancement along with the dislocation annihilation mechanism. Ultimately our aim has been to establish a scientific methodology for predicting the fatigue threshold levels, and interrogate on the dependence of the threshold on the microstructural features.

Another influential variable playing a decisive role in crack propagation is the variation of the strength of the crystal in which the dislocation glides as a result of the existing grain and twin boundaries. Owing to their strength, these boundaries behave as slip obstacles and introduce changes in the slip plane and in the Burgers vectors of the crack tip emitted dislocations *en-route*. Besides the obstacle effect of the boundaries, the characteristic dimensions of the microstructural features also play a key role in the cyclic FCG rate. These dimensions are important in such a way that they govern the spatial frequency of the grain/twin boundaries and the slip interactions on the active glide system. From a mechanistic view, all of these enlisted individual elements

will have profound contribution to the FCG, and therefore, their individual and concerted effects should be interrogated quantitatively to translate essential insight towards engineering structures with high fatigue impedance. In our previous work, we highlighted the role of coherent twins on the fatigue thresholds [13]. In this study, we turn our attention to the role of grain boundary types as discussed below.

## 1.2. Grain boundary characterization

As grain boundaries are decisive on the nature of the slip transmission reactions during the cyclic glide of the crack tip emitted dislocations, the characterization of grain boundaries is instrumental to quantify the resultant effects of these hierarchical structures on the FCG. To that end, an EBSD analysis is conducted to identify the representative microstructure of the as-received Ni-Co alloy which is experimented with a load ratio of  $R = K_{min}/K_{max} = 0.05$  and maximum stress level  $\sigma_{max} = 275$  MPa at room temperature as reported in our previous work [13]. In this study, we utilized Coincident Site Lattice (CSL) theory [19,20] to classify the types of the grain boundaries based on a misfit parameter  $\Sigma$  defined as the reciprocal of the number of the coincident atomic sites on the boundary. The measured frequencies of the different grain boundary types in the representative volume element of as-received Ni-Co alloy from the EBSD analysis are plotted in the histogram in Fig. 2. As can be seen, the most frequently observed boundaries are of  $\Sigma 3$ ,  $\Sigma 9$  and  $\Sigma 11$  types although the other types of boundaries are also present but to a lesser extent.

## 2. Theoretical background

### 2.1. Grain boundary types: CSL classification

Though the characterization of grain boundaries by the  $\Sigma$  parameter quantifies the continuity of the atomic lattice sites across a grain/twin boundary, to uniquely identify a grain boundary type, one has to know the relationship between the lattice orientations by means of the lattice rotation operations. To that end, in this work we will specify the grain boundary plane, the rotation axis and the misfit angle in addition to the  $\Sigma$  parameter. These three additional physical quantities are necessary and sufficient to uniquely characterize a specific grain boundary [21]. Throughout this work,  $\Sigma(\text{CSL no})\{h\ k\ l\}\langle p\ r\ s\rangle$  template is adopted to identify the grain boundary geometries uniquely. In this template employed, the plane  $\{h\ k\ l\}$  represents the crystallographic normal

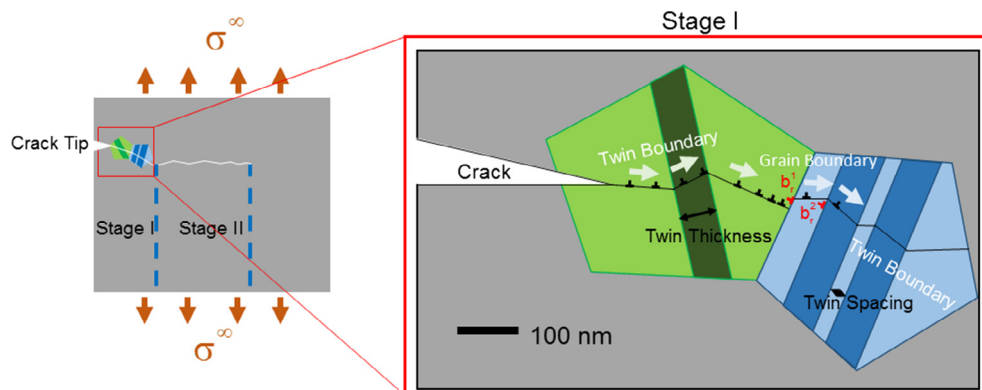


**Fig. 1.** The intragranular propagation mechanism for fatigue cracks at Stage I due to the shear driven irreversible cyclic glide of crack-tip emitted dislocations. The grain and twin boundaries encountered by the crack tip emitted dislocations on their cyclic glide trajectories incorporate or partially transmit these dislocations resulting cyclic plastic displacements at the crack tip. It is to be noted that in Stage II, the plastic region around the crack tip encloses numerous grains and the crack prefers to align its propagation direction normal to the tensile loading axis. This introduces a transition from Mode II or Mode III to a Mode I loading configuration for the loading geometry illustrated.

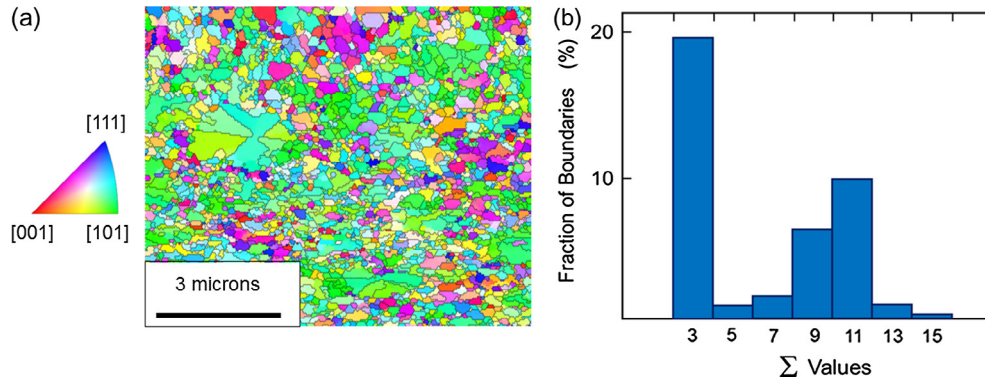


**Fig. 2.** (a) The EBSD orientation mapping of the nanocrystalline structure in as-received Ni-Co alloy. (b) The histogram plot of the fraction of boundaries observed in representative volume shown in (a). As can be seen, the most frequently seen boundaries are of  $\Sigma 3$ ,  $\Sigma 9$  and  $\Sigma 11$  types.

to the boundary plane which is of same indices in both of the local neighboring lattice coordinate frames. The direction,  $(p\ r\ s)$ , represents the rotation axis about which the second lattice is rotated with respect to the first lattice. Based on whether this rotation axis is normal or parallel to the boundary plane, the grain boundary type is denoted as twist or tilt.

In this work, we will focus on the interaction of crack tip emitted slip and the symmetric  $\Sigma 3\{1\ 1\ 1\}\langle 1\ 1\ 0\rangle$ ,  $\Sigma 9\{1\ 1\ 4\}\langle 1\ 1\ 0\rangle$ ,  $\Sigma 11\{1\ 1\ 3\}\langle 1\ 1\ 0\rangle$  tilt boundaries. At this stage, it should be emphasized that there are numerous possibilities for the geometry of the grain boundaries associated with a single CSL number [22–24]. Although we do not have a specific characterization data available for the determination of the spatial frequencies of the boundary types uniquely with their planes and misorientation angles, considering the  $\langle 1\ 1\ 0\rangle$  texture observed in the EBSD mapping of Fig. 2 and the low grain boundary energy of the symmetric tilt boundaries; the  $\Sigma 3\{1\ 1\ 1\}\langle 1\ 1\ 0\rangle$ ,  $\Sigma 9\{1\ 1\ 4\}\langle 1\ 1\ 0\rangle$ ,  $\Sigma 11\{1\ 1\ 3\}\langle 1\ 1\ 0\rangle$  boundaries stand out as the highest probable boundaries complying with the EBSD data provided in Fig. 2. Furthermore, ensuring the slip transmission across the boundary before the dislocation nucleation from the boundary in MD simulations plays a decisive role in focusing on these particular grain boundaries. On the other hand, the assumptive nature of this geometry preference utilized in the simulations throughout this work will be noted wherever it is necessary.

The first boundary type among these three boundaries focused on, shown in Fig. 3(a), is the coherent twin boundary, i.e.  $\Sigma 3\{1\ 1\ 1\}\langle 1\ 1\ 0\rangle$  which is a tilt boundary formed by a  $109.47^\circ$

rotation angle. For representation purposes, the atoms occupying the lattice sites with smallest centro-symmetry parameter [25] on the grain boundaries are shown in darker color compared to the other atoms inside the simulation box. The second most frequently observed boundary type is  $\Sigma 9\{1\ 1\ 4\}\langle 1\ 1\ 0\rangle$  which is illustrated in Fig. 3(b). This boundary is formed by rotating the lattice 2 about the axis  $\langle 1\ 1\ 0\rangle$  by an angle of  $38.94^\circ$  with respect to the lattice 1 across the boundary  $\{1\ 1\ 4\}$ . Lastly, as can be seen in Fig. 3(c),  $\Sigma 11\{1\ 1\ 3\}\langle 1\ 1\ 0\rangle$  boundary type is formed if lattice 2 is rotated about  $\langle 1\ 1\ 0\rangle$  axis by a right hand screw angle of  $50.47^\circ$  across the  $\{1\ 1\ 3\}$  plane with respect to lattice 1.

An important aspect of the presence of these grain boundaries on the mechanics of metal fatigue can be depicted as follows. The crack tip emitted dislocations can exhibit a numerous possible interactions with these boundaries manifested by the dislocation reactions and, as a result of these reactions, a prescribed magnitude of residual slip vector can reside at the grain boundary imposing a difference between the incoming and outgoing slip. Therefore, the accumulation of residual slip vectors do directly govern on the cyclic plastic displacement of the crack tip. The possible residual slip vectors are the products of the incoming slip and the corresponding grain boundary structure interactions which are closely linked with the CSL pattern on the grain boundary. From a perspective of the interface theory in crystalline materials, any residual dislocation residing on the grain boundary in a fashion conserving the CSL structure can be described by the shortest translation vectors of the displacement-shift complete lattice (DSC) which is the reciprocal lattice of the CSL structure [26,27].

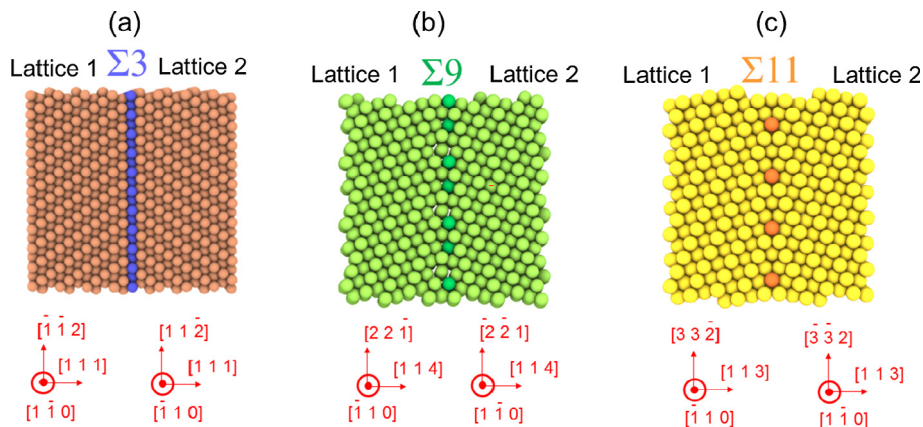


**Fig. 3.** (a) The bicrystal, lattice 1-lattice 2, formed by the coherent twin boundary  $\Sigma 3\{1\ 1\ 1\}\langle 1\ 1\ 0\rangle$  with the corresponding local lattice coordinate frames. (b) The bicrystal, lattice 1-lattice 2, formed by the  $\Sigma 9\{1\ 1\ 4\}\langle 1\ 1\ 0\rangle$  boundary with the corresponding local lattice coordinate frames. (c) The bicrystal, lattice 1-lattice 2, formed by the  $\Sigma 11\{1\ 1\ 3\}\langle 1\ 1\ 0\rangle$  boundary with the corresponding local lattice coordinate frames.

**Table 1**  
The base vectors of DSCL, i.e.  $\mathbf{e}_1^{\text{GB}}$ ,  $\mathbf{e}_2^{\text{GB}}$  and  $\mathbf{e}_3^{\text{GB}}$  in cubic crystal coordinate frame [28].

Boundary type	$\mathbf{e}_1^{\text{GB}}$	$\mathbf{e}_2^{\text{GB}}$	$\mathbf{e}_3^{\text{GB}}$
$\Sigma 3\{111\}\langle 110 \rangle$	$1/6[111]$	$1/6[-211]$	$1/6[-12-1]$
$\Sigma 9\{114\}\langle 110 \rangle$	$1/18[5-42]$	$1/18[-2-21]$	$1/18[114]$
$\Sigma 11\{113\}\langle 110 \rangle$	$1/22[4-71]$	$1/22[113]$	$1/22[33-2]$

Thus, any residual slip vector conserving the grain boundary structure can be described by the corresponding DSCL base vectors. Table 1 summarizes the DSCL base vectors  $\mathbf{e}_1^{\text{GB}}$ ,  $\mathbf{e}_2^{\text{GB}}$  and  $\mathbf{e}_3^{\text{GB}}$  in cubic crystal coordinate frame for  $\Sigma 3\{111\}\langle 110 \rangle$ ,  $\Sigma 9\{114\}\langle 110 \rangle$  and  $\Sigma 11\{113\}\langle 110 \rangle$  boundaries [28].

## 2.2. Quantification of fatigue crack threshold: a general view

For the threshold regime in which the microstructural features may prevail on the FCG rate, the primary cyclic crack advancement mechanism is the irreversible glide motion of crack-tip emitted dislocations along the active single slip system [29–31]. It is to be emphasized that at this stage of the FCG, the slip activity ahead of the crack tip is confined to only a few grains. The slip irreversibility is promoted by the residual slip vector accumulation during slip transfer across the grain boundaries and is suppressed by the annihilation of the positive and the negative sign dislocations emitted from the crack tip during loading and unloading portions of the cycle respectively. Furthermore, the backstress field formed by the emitted dislocations can introduce significant differences on the critical glide force required to initiate slip motion during the loading and the unloading cycle portions affecting the slip irreversibility in a complex fashion.

Considering the findings from the previous study of [32] addressing that the critical nucleation level for screw dislocations are lower than the edge dislocations at the crack tip and linked with this fact that the fatigue threshold is lower under Mode III loading conditions; in this work, we will impose Mode III loading conditions at the crack tip region and focus on modelling the irreversible cyclic glide of screw dislocations via the continuum scale dislocation motion simulations. To that end, the mechanical driving force for the FCG is quantified by the effective stress intensity factor range,  $\Delta K_{\text{eff}}$ , metric which is equal to the difference between the maximum,  $K_{\text{max}}$ , and the minimum,  $K_{\text{min}}$ , levels of the applied stress intensity factor, i.e.  $\Delta K_{\text{eff}} = K_{\text{max}} - K_{\text{min}}$ . We will implement a load ratio of  $R = K_{\text{min}}/K_{\text{max}} = 0.05$  and set the effective threshold value  $\Delta K_{\text{eff,th}}$  equal to a  $\Delta K_{\text{eff}}$  level sufficient to propagate the crack by a length of one Burgers vector,  $\Delta u = 1b$  ( $b = c/2|\langle 110 \rangle|$ ,  $c$ : lattice constant equal to 3.52 Å), which corresponds to 2.5 Å/cycle ( $2.5 \times 10^{-7}$  mm/cycle). The crack advancement rate of 1b/cycle is chosen on purpose of setting a finite  $\Delta K_{\text{eff,th}}$  value comparable with the experimental measurements [13]. Furthermore, the variation of  $\Delta K_{\text{eff}}$  for the cyclic crack growth rates ranging from 1b to 35b are also simulated within framework the dislocation motion simulations. An important point to emphasize is that during the modelling efforts we present, only the plastic activity ahead of the crack tip is considered, and the crack closure effects at the crack tip wake are neglected. Therefore, all the results are given as effective quantities complying with the driving force interpretation of  $\Delta K_{\text{eff}}$  employed in the experiments which are detailed in our previous work [13].

In our model, we will designate a hypothetically linear elastic, continuous medium in which the crack-tip emitted dislocations can glide and interact with the boundary types of  $\Sigma 3\{111\}\langle 110 \rangle$ ,  $\Sigma 9\{114\}\langle 110 \rangle$  and  $\Sigma 11\{113\}\langle 110 \rangle$ . The general configurations are illustrated for each interaction type in the subsequent sections. Meanwhile the glide resistance (or the lattice friction stress) inside a pristine crystal is identical for both the forward and the reverse glide, which will be denoted as  $\sigma_{\text{F}}$ ; the local fric-

tion stress varies at the grain boundaries *en-route* the forward and the reverse glide owing to the different slip transmission reaction energetics involved at the grain boundaries. Therefore, the glide resistance exerted on the dislocations within the very near proximity of the grain boundaries will be characterized by  $\sigma_{\text{F}}^{\text{forward}}$  and  $\sigma_{\text{F}}^{\text{reverse}}$  for the forward and the reverse glide respectively. The lattice friction stress values, corresponding to the crystal and the boundaries, will be evaluated by the Peierls-Nabarro (P-N) formulation within the framework of the MD simulations as will be explained in the next section.

## 2.3. Molecular Dynamics (MD) simulations and quantification of the friction stresses

The quantification of  $\sigma_{\text{F}}$ ,  $\sigma_{\text{F}}^{\text{forward}}$  and  $\sigma_{\text{F}}^{\text{reverse}}$  parameters requires a comprehensive knowledge about the details of the on-going slip transmission reactions. For this purpose, following the methodology in our previous works in the literature [13,33], we delineated a simulation box of approximately  $45 \times 108 \times 264 \text{ \AA}^3$  (the exact values are shown in Figs. 5–7 for each reaction scenario) with the periodic boundary conditions implemented in all three axes and introduced two equally spaced (88 Å) grain boundaries which are of either one of the  $\Sigma 3\{111\}\langle 110 \rangle$ ,  $\Sigma 9\{114\}\langle 110 \rangle$  or  $\Sigma 11\{113\}\langle 110 \rangle$  boundary types. The geometries of the simulation boxes utilized for the reaction scenarios are shown in Figs. 5–7. Moreover, we introduced a defect acting as a stress-concentrator to nucleate the dissociated  $1/2\langle 110 \rangle$  screw character dislocations and tracked the cyclic glide of the dislocations to quantify the change of their Burgers vectors and slip planes *en-route* owing to their interactions with the grain/twin boundaries. The interatomic forces are defined within framework of Folies-Hoyt Embedded Atom Method potential [34] at 10 K utilizing Nose-Hoover thermostat algorithm [35,36]. The MD simulations are conducted in LAMMPS (Large-scale Atomic/Molecular Massively Parallel Simulator).

Throughout the all MD simulations in this work, we employed NPT ensemble in which the number of atoms,  $N$ , the external pressure (at 1 bar),  $P$ , and the temperature,  $T$  (at 10 K), is held constant. Moreover, a fixed time step of  $10^{-3}$  picoseconds is implemented for each simulation. The number of time steps is varied for each scenario closely linked with the reaction type and the grain boundary involved. The defect is created by introducing a sessile perfect screw dislocation, of Burgers vector  $c/2\langle 110 \rangle$ , on  $\{112\}$ ,  $\{221\}$  and  $\{332\}$  planes perpendicular to grain boundaries of  $\Sigma 3\{111\}\langle 110 \rangle$ ,  $\Sigma 9\{114\}\langle 110 \rangle$  and  $\Sigma 11\{113\}\langle 110 \rangle$  respectively at a distance of 50 Å from the leftmost boundary of the simulation box. To create the defect, Eshelby-Stroh anisotropic formulation [25,37] is employed [38,39]. To quantify the lattice friction stress levels associated with the different slip transmission reactions, the P-N formulation is adopted. In the P-N formulation, the lattice friction stress level is calculated based on the maximum gradient of the total system energy,  $E^{\text{total}}$  (normalized with the corresponding slip vector magnitude  $b$ ), with respect to the disregistry displacement,  $u$ . This is formulated in Eq. (1) for the pristine crystal friction stress  $\sigma_{\text{F}}$ . It should be emphasized that an analogous formulation is followed to evaluate  $\sigma_{\text{F}}^{\text{forward}}$  and  $\sigma_{\text{F}}^{\text{reverse}}$  values as detailed in [13,33,40].

$$\sigma_{\text{F}} = \frac{1}{b} \max \left( \frac{\partial E^{\text{total}}}{\partial u} \right) \quad (1)$$

The total energy of the system is composed of both short range misfit energy,  $E^{\text{misfit}}$ , owing to the atomic level interaction across the active slip plane; and the long range terms of the elastic energy,  $E^{\text{elastic}}$  and the applied work,  $W$ , as expressed in Eq. (2). The individual energy terms are explicitly formulated in Eqs. (3)–(5)

$$E^{\text{total}} = E^{\text{misfit}} + E^{\text{elastic}} - W \quad (2)$$

$$E^{\text{misfit}} = \sum_{m=-\infty}^{+\infty} \gamma(f(ma' - u))a' \quad (3)$$

$$E^{\text{elastic}} = \frac{Gb^2}{4\pi} \ln \frac{R}{\xi} \quad (4)$$

$$W = \sigma_F b \quad (5)$$

where

$$f(ma' - u) = b_{\text{par}} + \frac{b_{\text{par}}}{\pi} \left\{ \tan^{-1} \left( \frac{ma' + 0.5u}{\xi} \right) + \tan^{-1} \left( \frac{ma' - 0.5u}{\xi} \right) \right\} \quad (6)$$

As can be seen in Eq. (3),  $E^{\text{misfit}}$  is directly linked with the energy pathway followed, (i.e. denoted as  $\gamma$  curve), during the glide or slip transmission phenomena.  $\gamma$  curve is a function of the disregistry function,  $f$ , which is expressed in Eq. (6) [41]. The disregistry function  $f$  conveys the information about the spatial distribution of the periodic shear displacements on the slip plane within the dislocation core neighborhood. The function  $f$  can be expressed in terms of six parameters  $b_{\text{par}}$ ,  $m$ ,  $a'$ ,  $w$ ,  $u$  and  $\xi$ . Among these parameters,  $b_{\text{par}}$  is the magnitude of the Shockley partials, i.e.  $|c/6 \langle 112 \rangle|$ ,  $m$  takes integer values and  $a'$  is the shortest periodicity distance between  $\{111\}$  glide planes in face centered cubic structure which is equal to  $2c/\sqrt{6}$ . The core half width parameter which prevails on  $E^{\text{misfit}}$  is denoted as  $\xi$ . It is to be noted that the core half width  $\xi$  is a function of the external stress tensor, the crystal structure, the character of the dislocation as well as the interatomic forces prevailing inside the crystalline. In this work, complying with the original P-N analysis, it is taken to be equal to the half of the  $\{111\}$  glide plane spacing, i.e.  $c/2\sqrt{3}$ . The long range  $E^{\text{elastic}}$  term is a function of both the elastic shear modulus,  $G = 50$  GPa, and  $\xi$ . It is worth emphasizing that  $E^{\text{elastic}}$  term is divergent for an infinite medium; therefore, it is evaluated within a radial domain size of  $R$  which is equal to  $500b$ . Furthermore, the outer core cut-off  $R$  is a constant; therefore, it does not contribute to the friction stress levels evaluated.

In the dislocation motion simulations,  $\Delta K_{\text{eff}}$  in Mode III is provided as an input for the system and the set of continuum scale equations describing the dislocation equilibrium are solved at each  $\Delta K_{\text{eff}}$  increment to find the threshold value corresponding to a finite magnitude of irreversible cyclic crack tip displacement, i.e.  $\Delta u = 1$  b/cycle. The simulations are delineated to cover both the initially pristine crystal and the crystal with the pre-existing slip (using continuum crystal dislocations the number of which are indicated as  $n_c$ ) configurations. In both of these cases, the dislocations are emitted from the crack tip when the local stress-intensity factor at the crack tip  $k_{\text{III}}$ , defined as in Eq. (7), reaches a critical value of  $k_{\text{IIIe}}$ , i.e. satisfying Eq. (8) [13].

$$k_{\text{III}} = K_{\text{III}} - \sum_{i=1}^n \frac{Gb_i}{\sqrt{2\pi r_i}} \cos \left( \frac{\theta_i}{2} \right) \quad (7)$$

$$k_{\text{III}} = \pm k_{\text{IIIe}} \quad (8)$$

In Eq. (7),  $r_i$  and  $\theta_i$  are the polar coordinates of the  $i^{\text{th}}$  dislocation with respect to the tip and  $n$  is the total number of dislocations residing inside the crystal. Careful examination of Eq. (7) addresses the fact that the local stress intensity factor,  $k_{\text{III}}$ , differs from the applied stress intensity factor,  $K_{\text{III}}$ , in presence of the dislocations ahead of the crack tip. This effect is denoted as shielding/anti-shielding if it degrades/promotes  $k_{\text{III}}$  with respect to  $K_{\text{III}}$ . On the

other hand, as can be seen in Eq. (8), the dislocations can be emitted both during the loading and the unloading portions of a fatigue cycle. Meanwhile the positive sign dislocations are emitted from the tip during loading, the negative sign dislocations are emitted during unloading. It should be noted that the positive and the negative sign dislocations attract and annihilate each other depending on the resultant force acting on them.

During the slip transmission across a grain boundary, the active slip systems and the Burgers vectors may differ across the boundary. Therefore, there are two sets of governing equations for the incoming slip in lattice 1 and the outgoing slip in lattice 2. Inside lattice 1, the glide plane is modelled as parallel to the crack surface complying with the Mode III loading geometry; on the other hand, the glide plane of the transmitted dislocations inside lattice 2 is determined based on the MD simulations and is dependent on the details of the slip transmission reactions accompanying. For lattice 1, the dislocation motion is governed based on the following expression in Eq. (9) [42,43]:

$$\frac{K_{\text{III}} b_i}{\sqrt{2\pi r_i}} \cos \left( \frac{\theta_i}{2} \right) + \sum_{i=1}^n \text{Re} \left( \frac{Gb_j \Phi}{4\pi \sqrt{x_i + \eta y_i}} \right) b_i - \frac{Gb_i}{4\pi r_i} \cos^2 \left( \frac{\theta_i}{2} \right) b_i - \lambda \frac{b_i}{4\pi \beta_i} - \sigma_F b_i = 0 \quad (9)$$

where

$$\Phi = \frac{1}{\sqrt{x_i + \eta y_i} + \sqrt{x_j + \eta y_j}} - \frac{1}{\sqrt{x_i + \eta y_i} + \sqrt{x_j - \eta y_j}} \quad (10)$$

In Eq. (10),  $\eta = \sqrt{-1}$ ,  $x_i$  and  $y_i$  are the position vector components for the  $i^{\text{th}}$  dislocation. The parameter  $\lambda$  describes the interaction of the screw dislocation with the grain boundary based on the formulation proposed by Stroh–Gemperlova [37,44] in which  $\beta_i$  is the distance between the  $i^{\text{th}}$  dislocation and the boundary. The parameter  $\lambda$  varies as 0, 0.078, 0.114 for Reaction 1, Reaction 2, Reaction 3 scenarios respectively as detailed in Appendix A. The details of these reactions will be further investigated in Sections 3.1.1–3.1.3. The general form of the dislocation motion equation in lattice 2 can be written as:

$$\frac{K_{\text{III}} b_i}{\sqrt{2\pi r_i}} \cos \left( \alpha - \frac{\theta_i}{2} \right) + \sum_{i=1}^n \text{Re} \left( \frac{Gb_j^2}{4\pi \sqrt{x_i + \eta y_i}} \Phi \right) \cos(\alpha) - \sum_{i=1}^n \text{Im} \left( \frac{Gb_j^2}{4\pi \sqrt{x_i + \eta y_i}} \Phi \right) \sin(\alpha) + \frac{Gb_i^2 (\sin(\alpha - \theta_i) - \sin \alpha)}{4\pi r_i \sin \theta_i} - \lambda \frac{b_i}{4\pi \beta_i} - \sigma_F b_i = 0 \quad (11)$$

where  $\alpha$  is the angle formed between the incipient slip plane, i.e. parallel to the crack flank, and the outgoing slip plane.

The general geometry and the individual force terms acting on the  $i^{\text{th}}$  dislocation are illustrated in Fig. 4 based on the expression in Eq. (9). It is to be noted that a very similar analogy can be also established for Eq. (11). Different from lattice 1, the active slip system in lattice 2 makes a finite angle of  $\alpha$  with the crack plane. Therefore, the expressions in Eqs. (9) and (11) exhibit differences in the geometrical factors. Although the forces acting due to the applied stress intensity  $K_{\text{III}}$  tends to drive a dislocation away from the crack tip, the traction-free surfaces of the crack and the crystal lattice friction apply restoring forces on it. The dislocation interaction force depends on the signs of the dislocations, they are repulsive/attractive for the same/different sign slip vectors. The image force acting on the dislocation due to the crystallographic orientation change across the grain boundary is of repulsive nature for the boundary types considered as detailed in Appendix A.

In this work, we have focused on three different reactions (in pairs of forward and reverse slip transmission) such that, there is

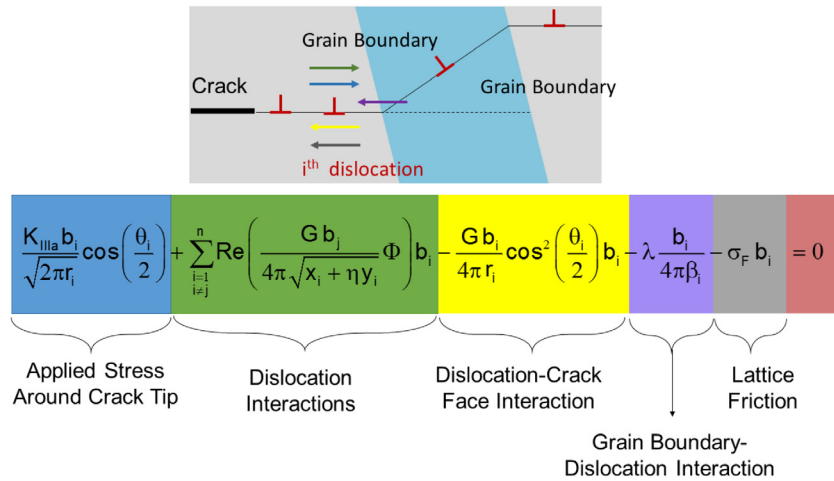


**Fig. 4.** The individual force terms acting on the  $i^{\text{th}}$  dislocation in lattice 1. The force terms are due to the applied stress intensity factor, the dislocation-dislocation interactions, the dislocation and the traction-free crack face interaction, the grain boundary – dislocation interaction and the lattice friction. It should be emphasized that for each  $K_{III}$  level applied, each dislocation irrespective of whether it is nucleated by crack-tip emission or it is contributing to the initial dislocation density (pre-existing slip) should be in force equilibrium as dictated by the right hand side of the equation.

one reaction for each of the  $\Sigma 3\{111\}\langle 110\rangle$ ,  $\Sigma 9\{114\}\langle 110\rangle$  and  $\Sigma 11\{113\}\langle 110\rangle$  type boundaries, i.e. Reaction 1, Reaction 2 and Reaction 3 respectively. The dislocation positions are solved numerically for each applied  $K_{III}$  value during the loading and the unloading cycle portions utilizing Eqs. (9)–(11). The cyclic plastic displacement at the crack tip is quantified based on the number of residual crack tip emitted dislocations, excluding the pre-existing crystal dislocations.

### 3. Effects of grain boundary types and slip transmission reactions on fatigue threshold

#### 3.1. Slip transmission reactions

##### 3.1.1. Reaction 1

In this work, the slip transmission across a  $\Sigma 3\{111\}\langle 110\rangle$  grain boundary has been studied in Reaction 1 scenario which focuses on the reversible cross-glide geometry as illustrated in Fig. 5. In order to simulate the transmission of a crack tip emitted screw dislocation across a  $\Sigma 3\{111\}\langle 110\rangle$  boundary, a defect has

been introduced at the initial configuration of the simulation box as can be seen in Fig. 5(a) in which OVITO visualization software is utilized [45]. This defect acts as a stress-concentrator and nucleates a dissociated screw dislocation of  $1/2[-110]_1$  which glides towards the  $\Sigma 3\{111\}\langle 110\rangle$  grain boundary. The dislocation reactions accompanying the slip transfer *en-route* the forward and reverse glide of the crack tip emitted slip has been detailed in Table 2. As can be seen in the insets of Fig. 5(b)–(e), the forward slip transfer introduces no residual slip vector on the  $\Sigma 3\{111\}\langle 110\rangle$  grain boundary. Similar behavior has been also observed during the reverse slip transfer from lattice 2 to lattice 1 across the boundary. Therefore, both the magnitudes of the residual slip vectors accompanying the forward and reverse slip transfers in Reaction 1 scenario (i.e.  $b_{r,forward}$  and  $b_{r,reverse}$ ) are equal to zero.

##### 3.1.2. Reaction 2

Reaction 2 scenario focuses on the transfer of a screw character slip across the symmetric tilt boundary of  $\Sigma 9\{114\}\langle 110\rangle$ . For this purpose, a simulation box is delineated with a defect which is introduced to nucleate a screw dislocation under the applied

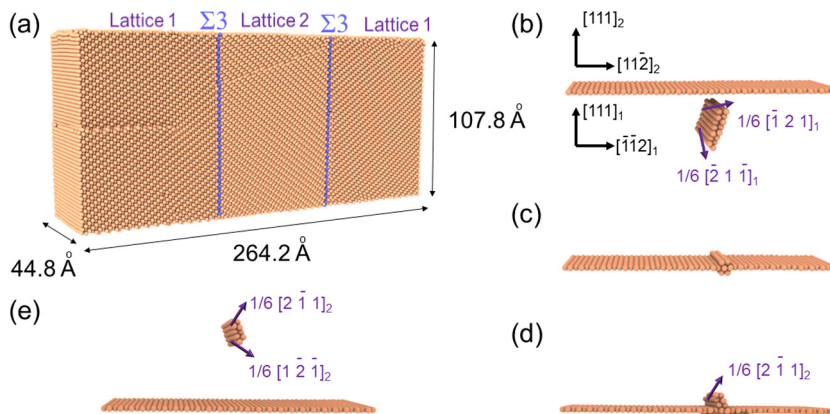


**Fig. 5.** (a) The simulation box utilized to simulate the reversible cross-slip reaction, namely Reaction 1. To nucleate the incoming dislocation towards the  $\Sigma 3\{111\}\langle 110\rangle$  boundary under the applied stress state, a defect is introduced in lattice 1. (b) The incoming dislocation of  $1/2[-110]_1$  dissociated into its Shockley partials of  $1/6[-21-1]_1$  and  $1/6[-121]_1$ . (c) The Shockley partials contract on the  $\Sigma 3\{111\}\langle 110\rangle$  boundary. (d) The contracted dislocation of  $1/2[-110]_1$ , is transmitted to lattice 2 in its dissociated form following a mirror symmetric glide trajectory across the boundary. Initially, the leading Shockley partial of  $1/6[2-11]_2$  is transferred to lattice 2 introducing a stacking fault layer between its core and the boundary. (e) Following the leading partial, a Shockley trailing partial is transmitted, i.e.  $1/6[1-2-1]_2$ . As a result, a dislocation of  $1/2[1-10]_2$  glides inside lattice 2 without leaving any residual Burgers vector on the boundary. Therefore, the forward reaction is a reversible cross-slip reaction. A similar reversible slip transfer mechanism is observed in an opposite fashion during unloading.

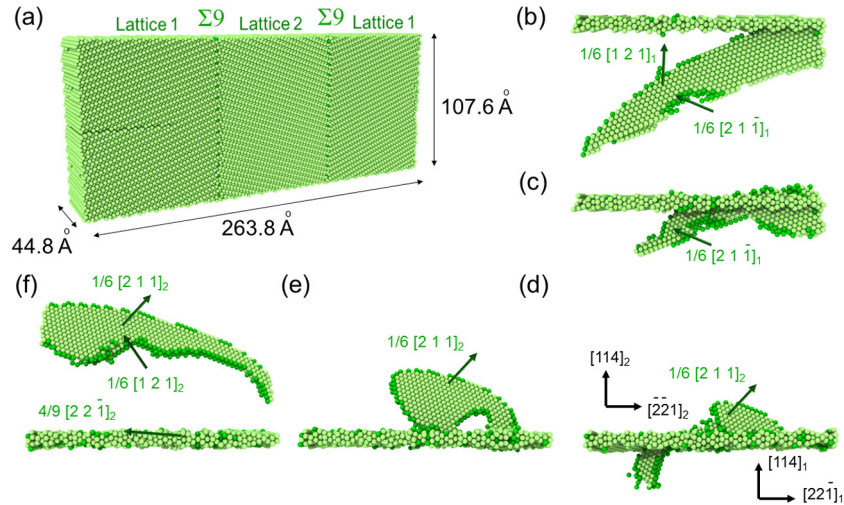


**Fig. 6.** (a) The simulation box utilized to simulate the forward slip transmission in Reaction 2 scenario. The incoming dislocation  $1/2[1 1 0]_1$  is dissociated into two Shockley partials,  $1/6[2 1 -1]_1$  and  $1/6[1 2 1]_1$ . (b) and (c) The interaction of the leading partial  $1/6[2 1 -1]_1$  and the trailing partial  $1/6[1 2 1]_1$  with  $\Sigma 9\{1 1 4\}\langle 1 1 0 \rangle$  boundary respectively. (d) The incorporated  $1/2[1 1 0]_1$  dislocation into  $\Sigma 9\{1 1 4\}\langle 1 1 0 \rangle$  grain boundary dissociates into  $4/9[2 2 -1]_2$  which is a glissile grain boundary dislocation for the  $\Sigma 9\{1 1 4\}\langle 1 1 0 \rangle$  grain boundary and makes the boundary nucleate a glissile dislocation of  $1/2[1 1 0]_2$  into lattice 2. (e) and (f) Captions from the glide trajectory of the transmitted  $1/2[1 1 0]_2$  dislocation inside lattice 2.  $1/2[1 1 0]_2$  dissociates into two Shockley partials, i.e., the leading partial  $1/6[2 1 1]_2$  and the trailing partial  $1/6[1 2 1]_2$ .

loading, as exhibited in Fig. 6(a). In this case, the incoming dissociated screw dislocation of  $1/2[1 1 0]_1$  incorporates into the boundary from lattice 1 side and the resulting strain energy introduced into the medium is relaxed by nucleating a  $1/2[1 1 0]_2$  screw dislocation inside lattice 2 along with a residual slip vector of  $4/9[2 2 -1]_2$  which is a grain boundary dislocation of DSCL and does not change the CSL index. This is illustrated in the insets of Fig. 6(b)–(f). The details of the forward and reverse slip transfer across the  $\Sigma 9\{1 1 4\}\langle 1 1 0 \rangle$  boundary are given in Table 2. As can be seen in Fig. 6(e), the forward slip transfer is irreversible with a residual slip vector of  $b_{r,forward} = 4/9[2 2 -1]_2$ . Similarly, the reverse slip transfer across the  $\Sigma 9\{1 1 4\}\langle 1 1 0 \rangle$  boundary is also of irreversible nature in Reaction 2 scenario, i.e.  $b_{r,reverse} = 4/9[-2 -2 1]_1$ .

### 3.1.3. Reaction 3

The last reaction scenario focused in this work, i.e. Reaction 3, consists of the transfer of slip across the  $\Sigma 11\{1 1 3\}\langle 1 1 0 \rangle$  symmetric tilt boundary. During the forward slip transmission from lattice 1 to lattice 2, the incoming screw character dislocation of  $1/2[-101]_1$  interacts with the grain boundary as detailed in Table 2. Similar to the other scenarios, the dislocation is nucleated from a defect located inside lattice 1 region of the simulation box as illustrated in Fig. 7(a). The slip-grain boundary interaction for Reaction 3 involves the incorporation of the incoming slip and the transmission of a screw dislocation of  $1/2[1 1 0]_2$  into lattice

2. It should be noted that this slip transfer is accompanied with a residual slip vector of  $b_{r,forward} = -1/22[4 - 7 1]_2$  which is a grain boundary dislocation of DSCL. Similarly, a set of irreversible dislocation reactions accompany the slip transfer from lattice 2 to lattice 1 as expressed in Table 2 leaving a residual slip vector of  $b_{r,reverse} = 2/22[3 3 -2]_1$ . As can be seen in Table 1,  $b_{r,reverse}$  is also a grain boundary dislocation belonging to the group of shortest translation vectors of DSCL.

### 3.2. Variation of the friction stresses based on the grain boundary structure and the slip transfer reactions

The transmission of the crack tip emitted slip across the grain boundaries is governed by the structure of the boundary and the applied loading configuration as well as the incoming slip geometry, i.e. glide direction and plane. The details of these dislocation reactions focused in this work are described in Table 2. The corresponding lattice friction stress values are tabulated in Table 3 for each reaction type distinguishing between the forward and the reverse glide. It is worth emphasizing that the lattice friction stress is evaluated to be equal to 60 MPa inside the pristine crystal along the  $\langle 1 1 0 \rangle \{1 1 1\}$  slip system family.

As can be seen in Tables 2 and 3 for Reaction 1 which is a reversible cross-glide reaction across the  $\Sigma 3\{1 1 1\}\langle 1 1 0 \rangle$  coherent twin boundary, there is no friction stress differential, i.e. defined as

**Table 2**

The dislocation reactions resulting from the MD simulations corresponding to different loading and boundary type configurations. The subindices “1” and “2” indicate the local crystallographic coordinate frames attached to lattice 1 and lattice 2 for the boundary types of  $\Sigma 3\{1 1 1\}\langle 1 1 0 \rangle$ ,  $\Sigma 9\{1 1 4\}\langle 1 1 0 \rangle$  and  $\Sigma 11\{1 1 3\}\langle 1 1 0 \rangle$ . The grain boundary dislocations, i.e. residual dislocations, which are linearly dependent on DSCL base vectors are distinguished from the lattice dislocations by the superscript GB.

$\Sigma 3\{1 1 1\}\langle 1 1 0 \rangle$	$\Sigma 9\{1 1 4\}\langle 1 1 0 \rangle$	$\Sigma 11\{1 1 3\}\langle 1 1 0 \rangle$
<b>Reaction 1</b>	<b>Reaction 2</b>	<b>Reaction 3</b>
<b>Forward</b>	<b>Forward</b>	<b>Forward</b>
$1/6[-2 1 -1]_1 + 1/6[-1 2 1]_1 \rightarrow 1/2[-1 1 0]_1$	$1/6[2 1 -1]_1 + 1/6[1 2 1]_1 \rightarrow 1/2[1 1 0]_1$	$1/6[2 1 -1]_1 + 1/6[1 -1 -2]_1 \rightarrow 1/2[1 0 -1]_1$
$1/2[-1 1 0]_1 \rightarrow 1/2[1 -1 0]_2$	$1/2[1 1 0]_1 \rightarrow 1/2[1 1 0]_2 + 4/9[2 2 -1]_2^{GB}$	$1/2[1 0 -1]_1 \rightarrow 1/22[-15 -4 -1]_2$
$1/2[1 -1 0]_2 \rightarrow 1/6[1 -2 -1]_2 + 1/6[2 -1 1]_2$	$1/2[1 1 0]_2 \rightarrow 1/6[2 1 1]_2 + 1/6[1 2 1]_2$	$1/22[-15 -4 -1]_2 \rightarrow 1/2[-1 -1 0]_2 + 1/22[-4 7 -1]_2^{GB}$
<b>Reverse</b>	<b>Reverse</b>	<b>Reverse</b>
$1/6[1 -2 -1]_2 + 1/6[2 -1 1]_2 \rightarrow 1/2[1 -1 0]_2$	$1/6[2 1 1]_2 + 1/6[1 2 1]_2 \rightarrow 1/2[1 1 0]_2$	$1/2[-1 -1 0]_2 \rightarrow 1/6[-2 -1 1]_2 + 1/6[-1 -2 -1]_2$
$1/2[1 -1 0]_2 \rightarrow 1/2[-1 1 0]_1$	$1/2[1 1 0]_2 \rightarrow 1/2[1 1 0]_1 + 4/9[-2 -2 1]_1^{GB}$	<b>Reverse</b>
$1/2[-1 1 0]_1 \rightarrow 1/6[-2 1 -1]_1 + 1/6[-1 2 1]_1$	$1/2[1 1 0]_1 \rightarrow 1/6[2 1 -1]_1 + 1/6[1 2 1]_1$	$1/6[-2 -1 1]_2 \rightarrow 1/6[1 -1 2]_1 + 1/22[7 -4 -1]_2^{GB}$
		$1/6[-1 -2 -1]_2 \rightarrow 1/6[-2 -1 -1]_1 + 2/22[3 3 2]_1^{GB}$
		$1/6[1 -1 2]_1 + 1/6[2 1 1]_1 \rightarrow 1/2[1 0 1]_1$

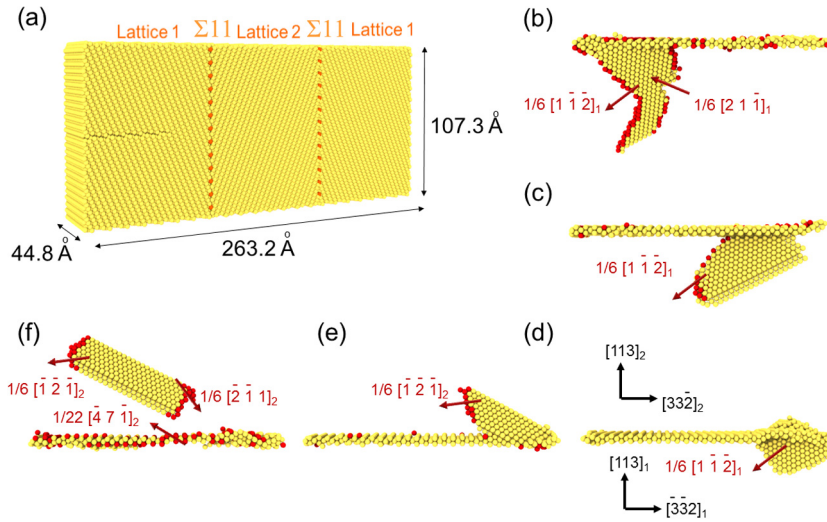


**Fig. 7.** (a) The simulation box utilized to study the forward slip transmission in Reaction 3 scenario across the  $\Sigma 11\{1\ 1\ 3\}\{1\ 1\ 0\}$  boundary. The dislocation is nucleated from the defect under applied shear loading and tracked along the glide trajectory in both grains during loading and unloading. (b) The image caption for the interaction of the incoming dissociated dislocation of  $1/2[1\ 0\ -1]_1$  with the  $\Sigma 11\{1\ 1\ 3\}\{1\ 1\ 0\}$  boundary. (c) After incorporating the leading partial  $1/6[2\ 1\ -1]_1$ , the trailing partial  $1/6[1\ -1\ -2]$  interacts with the grain boundary. (d) The incorporation of the leading and trailing partials introduce the grain boundary dislocation of  $1/22[-4\ 7\ -1]_2$  which is glissile on the  $(1\ 1\ 3)$  grain boundary plane. (e) In order to further release the accumulated strain energy, the  $\Sigma 11$  grain boundary emits a dissociated dislocation of  $1/2[-1\ -1\ 0]_2$  into lattice 2. The leading partial of  $1/6[-1\ -2\ -1]_2$  is shown in the inset. (f) Following the leading partial, the trailing partial of  $1/6[-2\ -1\ 1]_2$  is also emitted into lattice 2 and under the applied stress, the dissociated dislocation glides further away from the boundary.

$\Delta\sigma = |\sigma_F^{\text{barrier-forward}} - \sigma_F^{\text{barrier-reverse}}|$ , unlike the other reactions. Moreover, the absence of the residual slip vector for this reaction during the forward and the reverse slip transmissions are expected to promote the fatigue threshold. On the other hand, for the other reactions, depending on the magnitude of the incoming and outgoing slip vectors, the lattice friction values show significant discrepancies along with the varying residual slip vectors. These resulting data suggest that in addition to  $\sigma_F^{\text{forward}}$  and  $\sigma_F^{\text{reverse}}$ , both  $\Delta\sigma$  and the scalar sum of the residual slip vectors corresponding to the forward and the reverse glide,  $|b_{r,\text{forward}}| + |b_{r,\text{reverse}}|$ , should be also considered to model the fatigue threshold behavior of nanocrystalline Ni-Co.

### 3.3. Microstructure sensitivity of fatigue threshold

The effective fatigue threshold values,  $\Delta K_{\text{eff,th}}$ , evaluated based on the dislocation motion simulations are supplemented with the modified P-N formulation. The results are plotted in Fig. 8 for the initially pristine ( $n_c = 0$ ) and the pre-existing slip ( $n_c = 4$ ) configurations respectively. The pre-existing slip is simulated by inserting the continuum crystal dislocations ahead of the crack tip in the dislocation motion simulations. For each of the reaction types analyzed, the grain size values are varied within the range of 10–60 nm equally, (i.e. denoted as  $d$ ). As can be seen; although the  $\Delta K_{\text{eff,th}}$  values exhibit significant differences regarding the reversibility of the slip transmission across the grain boundaries

**Table 3**

The lattice friction values evaluated within Peierls-Nabarro framework for the forward and reverse glide across the corresponding the grain boundaries for the given reaction types.

	Forward	Reverse
Reaction 1 $\Sigma 3\{1\ 1\ 1\}\{1\ 1\ 0\}$	$\sigma_F^{\text{forward}} = 145$ MPa	$\sigma_F^{\text{reverse}} = 145$ MPa
Reaction 2 $\Sigma 9\{1\ 1\ 4\}\{1\ 1\ 0\}$	$\sigma_F^{\text{forward}} = 265$ MPa	$\sigma_F^{\text{reverse}} = 310$ MPa
Reaction 3 $\Sigma 11\{1\ 1\ 3\}\{1\ 1\ 0\}$	$\sigma_F^{\text{forward}} = 294$ MPa	$\sigma_F^{\text{reverse}} = 203$ MPa

based on the reaction geometry involved, the decrease of the characteristic dimension  $d$  promotes the fatigue resistance for all of the reaction types considered. This shows that the grain size effect on the cyclic slip irreversibility is of long range nature and it governs on the dislocation interaction distances and the extent of pile-ups unlike the short-range contribution of the grain boundary barrier strength. On the other hand, it is important to emphasize that the short-range effects due to the varying slip energetics linked with the different grain boundary structures can also contribute to the FCG behavior in the threshold regime. This effect can be observed in the finite  $\Delta K_{\text{eff,th}}$  differentials shown in Fig. 8.

As the TEM images in our previous work [13] present evidence for the crystal dislocations in the undeformed configuration of Ni-Co remnant from the electrodeposition process, the shielding/anti-shielding effects of these defects should also be incorporated in our analyses to develop a comprehensive understanding of the microstructural effects on the fatigue threshold levels. Therefore, the dislocation motion simulations are also conducted by introducing 4 crystal dislocations,  $n_c = 4$ , ahead of the crack tip inside the delineated medium. This allowed us to quantify the effects of the pre-existing slip on fatigue behavior and compare the resulting  $\Delta K_{\text{eff,th}}$  values of the pristine crystal, (i.e.  $n_c = 0$ ), illustrated in Fig. 8(a) and of the pre-existing slip in Fig. 8(b). The crystal dislocations ahead of the crack tip promote the fatigue resistance compared to the pristine crystallite scenarios as can be seen in Fig. 8 since the stress field created by the positive crystal dislocations suppresses the slip irreversibility by decreasing both the number of dislocations emitted from the crack and the dislocation mean glide path which governs on the frequency of the dislocation grain boundary interactions along the glide trajectory with the back-stress effects. Another important point to emphasize is that the shielding effect prevails irrespective of the short-range nature of the slip transmission reactions although the extent of it varies.

### 3.4. A closed form, predictive equation for the microstructure-sensitive fatigue threshold

The dislocation motion simulation results presented in Fig. 8 suggest that the slip-transmission configuration, the pre-existing

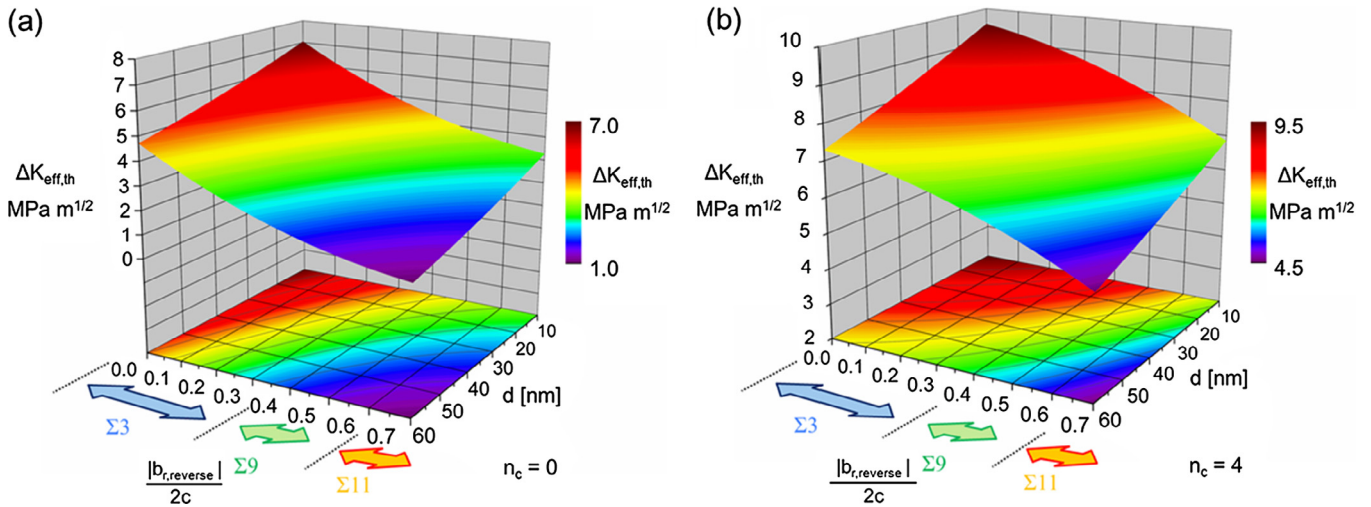


**Fig. 8.** (a) The variation of  $\Delta K_{\text{eff,th}}$  with the residual Burgers vector magnitude and the grain size in the absence of pre-existing slip, i.e.  $n_c = 0$ . (b) The variation of  $\Delta K_{\text{eff,th}}$  with the residual Burgers vector magnitude,  $|b_{r,\text{reverse}}|$  and the grain size,  $d$ , in presence of the pre-existing slip equal to 4 crystal dislocations, i.e.  $n_c = 4$ .

slip (the crystal dislocations) and the characteristic dimension, (i.e. the size of the grains), contribute to the threshold value in a concerted fashion. In this work,  $\Delta K_{\text{eff,th}}$  is quantified based on the friction stresses  $\sigma_F$ ,  $\sigma_F^{\text{forward}}$  and  $\sigma_F^{\text{reverse}}$ , the total residual slip vector, (i.e.  $|b_{r,\text{forward}}| + |b_{r,\text{reverse}}|$ ), the friction stress differential across the grain boundaries, (i.e.  $\Delta\sigma = |\sigma_F^{\text{forward}} - \sigma_F^{\text{reverse}}|$ ), and the number of crystal dislocations,  $n_c$ . Following the multi-variable regression of the results presented in Tables 2 and 3 along with the data presented in Fig. 8, a closed form equation is proposed to predict the effective threshold  $\Delta K_{\text{eff,th}}$  for Ni-Co alloy where  $\Delta K_0$  is taken as equal to  $1 \text{ MPa}\sqrt{\text{m}}$  and  $n_0 = 1$ :

$$\frac{\Delta K_{\text{eff,th}}}{\Delta K_0} = 4.36 \sqrt{\frac{\sigma_F^{\text{forward}}}{\sigma_F}} - 0.21 \sqrt{\frac{d}{b}} + 0.76 \frac{n_c}{n_0} - 0.37 \sqrt{\frac{|b_{r,\text{forward}}| + |b_{r,\text{reverse}}|}{b}} - 3.58 \sqrt{\frac{\sigma_F^{\text{forward}} - \sigma_F^{\text{reverse}}}{\sigma_F}} \quad (12)$$

### 3.5. Comparison of the predicted $\Delta K_{\text{eff}}$ values with the experimental measurements

Fig. 9 shows the threshold bounds established by incorporating the different grain boundary structures in the dislocation motion simulations under varying  $\Delta u$  values for a range of  $d$  values varying between 10 and 60 nm. The experimental measurements of the crack growth rates for the as received Ni-Co and the 600 °C 4 h annealed Ni-Co 600 HT samples fall into different bounds at different growth rates complying with the distinct slip irreversibility ratios of the slip transmission reactions across the  $\Sigma 3\{111\}\langle 110\rangle$ ,  $\Sigma 9\{114\}\langle 110\rangle$  and  $\Sigma 11\{113\}\langle 110\rangle$  grain boundary structures. Since the as-received and the annealed samples exhibit different initial dislocation densities, the number of crystal dislocations are changed in modelling the Stage I behavior of these two materials in which  $n_c = 1$  and  $n_c = 4$  are used respectively. The lack of a unique threshold value originates from the fact that a short length fatigue crack (following the initiation stage) encounters with varying boundary structures and its growth rate varies significantly owing to the different slip transmission characteristics of the grain boundaries present in the microstructure. Therefore, within a small range of  $\Delta K_{\text{eff}}$  variation, a significant change in the crack growth rate can be measured. This suggests that we

can only speak of an interval of  $\Delta K_{\text{eff,th}}$  values instead of a unique value for a given material owing to the distinct response of the microstructural features, such as the grain boundary structure and the grain size, into the cyclic glide of the dislocations emitted from the crack tip. Moreover, the pre-existing slip (initial dislocation density) is also shown to be considerably promoting the FCG impedance of Ni-2.89 wt.% Co.

## 4. Discussion of the results

The nature of the interaction between the slip and the different boundary types has been the subject of the several previous experimental and theoretical investigations [2,26,40,46,47]. The coherent twin boundaries, (i.e.  $\Sigma 3\{111\}\langle 110\rangle$ ), are known to impart significant FCG resistance to the nano-architected microstructures involved for the coherent twin boundary geometry is closely linked with the symmetry and the low CSL number indicating the lattice continuity across the boundary. These characteristic features are the prominent factors behind the high threshold values measured as also shown theoretically in our dislocation motion simulations for Reaction 1. The symmetric tilt  $\Sigma 9\{114\}\langle 110\rangle$  type grain boundary bears characteristic similarities with the coherent twin boundary,  $\Sigma 3\{111\}\langle 110\rangle$ , as both of them are the members of a more general class of  $\Sigma 3^n$  boundaries which are known to be capable of conjoining [48]. On the other hand, the slip energetics and the slip reversibility are significantly different for the  $\Sigma 9$  and  $\Sigma 3$  type boundaries as shown in the previous literature [27,49] complying with the results of the MD simulations and the P-N analyses presented in this work. As can be seen in Fig. 8, in both the pristine crystalline and the pre-existing slip configurations, the threshold values are higher for the delineated microstructures composed of  $\Sigma 3\{111\}\langle 110\rangle$  boundaries than the other microstructures. The lower fatigue resistance of the microstructures with the  $\Sigma 9\{114\}\langle 110\rangle$  grain boundaries finds its roots in the higher slip irreversibility and the greater slip stress differentials,  $\Delta\sigma$ , associated with the nature of the slip transmission reactions across these boundaries compared to the coherent twin boundaries.

The dislocation motion simulations constituting the  $\Sigma 11\{113\}\langle 110\rangle$  type boundaries, are distinguished by their lower fatigue resistance values compared to the other configurations analyzed in this work. The larger  $\Delta\sigma$  differential and the greater magnitude of the resultant residual slip vector are the major mechanical

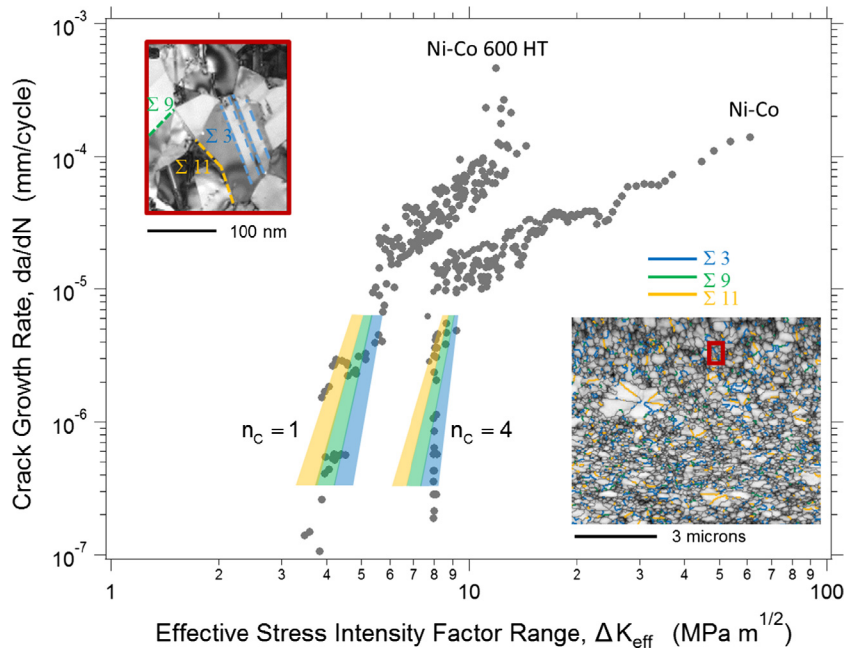


**Fig. 9.** The microstructure dependence of the theoretical fatigue threshold behavior of Ni-2.89 wt.% Co in comparison with the experimental data corresponding to as received Ni-Co and annealed (600 °C for 4 h) Ni-Co 600 HT. As can be seen, modelling the variation of the grain boundary character ahead of the crack tip in dislocation motion simulations results in threshold bounds within the characteristic dimension range of 10–60 nm. The highest and lowest cyclic slip irreversibility is observed for the delineated geometries and microstructures favoring Reaction 3 and Reaction 1. Similar behavior can be also extended for the different crack growth rates within Stage I regime. It should be emphasized that the pre-existing slip (modeled by introducing crystal dislocations) significantly promotes the FCG impedance. The considerable contribution of pre-existing slip on the threshold level is evident from the comparison of Ni-Co and Ni-Co 600 HT Stage I behavior.

factors in explaining the lower  $\Delta K_{\text{eff,th}}$  values corresponding to the simulation scenarios favoring Reaction 3 slip transmission geometry. It should be emphasized that the lower continuity level of the atomic lattice sites across the  $\Sigma 11$  type boundaries might be the crystallographic reason underlying this behavior which was also observed in the earlier slip trace transmission experiments of Lim et al. [50]. Therefore, even though the barrier strength values for the symmetric tilt  $\Sigma 11\{1\ 1\ 3\}\langle 1\ 1\ 0\rangle$  boundary are higher compared to the other boundaries analyzed, the slip irreversibility associated with the grain boundary slip transmission reactions is expected to dominate the fatigue threshold levels of the microstructures constituting the  $\Sigma 11\{1\ 1\ 3\}\langle 1\ 1\ 0\rangle$  boundary. On the other hand, it is to be noted that further studies are necessary in order to examine the behavior of other grain boundaries classified by the  $\Sigma 11$  CSL number.

The atomistic scale calculations are conducted via an interatomic potential of pure Ni which might introduce a small variation in the barrier strength calculations compared to the original composition of Ni-2.89 wt.% Co. It is known that the Co composition in Ni-Co alloys can contribute to the unstable stacking fault energy,  $\gamma^{\text{us}}$ , and the intrinsic stacking fault energy,  $\gamma^{\text{isf}}$ , levels as shown by Chowdhury et al. [8] via the molecular statics simulations and the ab initio calculations. The same study shows that the magnitude of the residual slip vector is the governing parameter on the generalized stacking fault energy levels associated with the slip transmission reactions which is surmised to be of the same nature in both pure Ni and Ni-2.89 wt.% Co. To that end, we expect the current slip energetics calculations to be of well representative. On the other hand, for the alloys with high Co concentration, segregation mechanisms [51] can introduce significant changes both in the barrier strength and the kinetics of the slip transmission reactions.

The simulation results suggest that the pre-existing slip is a prominent microstructural parameter to be considered in assessing the fatigue threshold resistance. The detailed comparison of the

resulting threshold levels between the pristine crystalline and the delineated configurations of the pre-existing slip in Fig. 8, suggests that substantial increase in  $\Delta K_{\text{eff,th}}$  is possible in presence of the pronounced crack tip shielding owing to the crystal dislocations which is confirmed to be present for the electrodeposited Ni-Co alloy samples imaged by TEM in our previous work [13]. Furthermore, the dislocation motion simulation results show that the promotion of the FCG impedance in presence of the pre-existing slip is observed for all of the reaction types analyzed irrespective of the differences in the short-range grain boundary slip transmission characteristics involved. This behavior complies with the long-range nature of the crystal dislocation induced elastic fields suppressing the local stress intensity at the crack tip.

The grain size is also an influential microstructural parameter for the FCG resistance in the threshold regime. As can be seen in Fig. 8, the refined grain size introduces significant increase in  $\Delta K_{\text{eff,th}}$ . This behavior can be explained based on the shorter cyclic mean free path of the crack tip emitted dislocations in response to the higher frequency of the slip barriers for microstructures with finer grain sizes. Provided their shorter glide path, the dislocations can more easily slip back to the tip which in turn promotes the fatigue resistance as reflected by the  $\Delta K_{\text{eff,th}}$  levels.

In this work, we employed a multiscale approach to model the contribution of cyclic slip and grain boundary interplay on the FCG of materials the microstructure of which is fashioned with the grain and twin boundaries at nanoscale. Extracting the lattice friction parameters by characterizing the slip energetics involved for the dislocation glide inside a pristine crystalline and glide transmission across a specific grain boundary within the framework of MD simulations and afterwards incorporating these parameters as input for the continuum scale dislocation equilibrium equations suggest promising results for understanding the microstructure effects prevailing on the FCG. At this stage, it should be emphasized that the results should be assessed within the limits of the governing equations, including the 2-D linear elastic constitutive

behavior, the prevalent crack growth mechanism being the cyclic slip irreversibility along a single active slip system, the symmetric tilt grain boundary types considered and the interatomic forces potential employed. To that end, a unified modelling approach which can also incorporate a vast spectrum of geometries, the boundary types as well as the different alloy compositions would provide a sophisticated tool for architecting microstructures with higher FCG impedance complying with the demands of the new horizon technologies.

## 5. Conclusion

Following conclusions are drawn from this work:

- (1) The slip transmission characteristics of the grain boundaries play a dominant role in the fatigue threshold levels of nanocrystalline Ni-2.89 wt.% Co alloy. It has been shown theoretically (within the framework of the MD simulations and the P-N formulation) that among the 3 types of symmetric tilt boundaries studied,  $\Sigma 3\{1\ 1\ 1\}\langle 1\ 1\ 0\rangle$ ,  $\Sigma 9\{1\ 1\ 4\}\langle 1\ 1\ 0\rangle$  and  $\Sigma 11\{1\ 1\ 3\}\langle 1\ 1\ 0\rangle$ ; the highest and the lowest fatigue resistances are evaluated in the microstructures composed of the  $\Sigma 3\{1\ 1\ 1\}\langle 1\ 1\ 0\rangle$  and  $\Sigma 11\{1\ 1\ 3\}\langle 1\ 1\ 0\rangle$  type boundaries respectively.
- (2) As a characteristic dimension, the grain size is shown to have a significant effect on the fatigue crack impedance of nanocrystalline Ni-2.89 wt.% Co alloy. The refinement in the grain size (within range of 60 nm to 10 nm) is shown to promote higher fatigue threshold levels for the symmetric tilt  $\Sigma 3\{1\ 1\ 1\}\langle 1\ 1\ 0\rangle$ ,  $\Sigma 9\{1\ 1\ 4\}\langle 1\ 1\ 0\rangle$  and  $\Sigma 11\{1\ 1\ 3\}\langle 1\ 1\ 0\rangle$  boundaries.
- (3) The pre-existing slip is theoretically shown to impart higher FCG impedance in nanocrystalline Ni-2.89 wt.% Co alloy compared to the pristine crystalline configuration. This shielding effect on the crack tip stress fields retard the crack propagation irrespective of the structures of the grain boundaries present ahead of the crack tip.
- (4) The dislocation motion simulations supplemented by the atomistic scale slip energetics calculations (within the framework of P-N formulation) are shown to be capable of determining the fatigue threshold bounds associated with the different grain boundary types and the pre-existing slip. The resulting threshold bounds are in close agreement with the experimental crack growth rate measurements of the nanocrystalline Ni-2.89 wt.% Co alloy.

## Acknowledgments

The support from Nyquist Chair funds is gratefully acknowledged.

## Appendix A. Forces on dislocations near an interface

In this section, a detailed insight into the quantification of the forces acting on the dislocations posited near an interface formed

by two anisotropic crystals will be provided. This analysis plays a critical role in determination of the forces acting on the incoming and outgoing slip across a specific grain boundary within the framework of continuum formulation introduced in Eqs. (9)–(11). Firstly, the fourth order elastic stiffness tensor is constructed based on the EAM Ni potential utilized in MD simulations [34]. Within the framework of this potential, the three independent elastic constants of Ni in cubic coordinate system  $\mathbf{E}_1 - \mathbf{E}_2 - \mathbf{E}_3$  ( $\equiv [1\ 0\ 0] - [0\ 1\ 0] - [0\ 0\ 1]$ ), with a lattice constant of 3.52 Å, are equal to:  $C_{1111}^* = 240.6$  GPa,  $C_{1122}^* = 150.3$  GPa,  $C_{1212}^* = 119.2$  GPa.

The fourth order elastic tensor in the cubic crystal frame is transformed to the dislocation frame before being utilized as an input for the quantitative analysis of the grain boundary - dislocation interactions. The dislocation frame is constructed by the orthonormal base vectors of  $\mathbf{e}_1 - \mathbf{e}_2 - \mathbf{e}_3$  in which  $\mathbf{e}_2$  is the glide plane normal and  $\mathbf{e}_3$  is parallel to the glide direction, i.e. the normalized Burgers vector.  $\mathbf{e}_1$  is determined by the vector cross-product of  $\mathbf{e}_2$  and  $\mathbf{e}_3$ , i.e.  $\mathbf{e}_1 = \mathbf{e}_2 \times \mathbf{e}_3$ . The corresponding glide systems activated for the incoming and outgoing slip in Reactions 1, 2 and 3 scenarios are tabulated in Table A.1.

The elastic stiffness tensor is transformed to the dislocation frame in lattice 1 (or similarly lattice 2) based on the coordinate transformation rules of a fourth order tensor as shown in Eq. (A.1):

$$C_{ijkl} = C_{pqrs}^* Q_{ip} Q_{jq} Q_{kr} Q_{ls} \quad (\text{A.1})$$

where the summation convention is implied on repeating indices and all of the indices are varied from 1 to 3. The transformation matrix  $Q_{ij}$  is constructed by the dot product of  $\mathbf{E}_i$  and  $\mathbf{e}_j$  base vectors as follows:

$$Q_{ij} = \mathbf{E}_i \cdot \mathbf{e}_j \quad (\text{A.2})$$

The general displacement field solution of Eshelby et al. [25] for an anisotropic, linear elastic medium is given in Eq. (A.3) provided that Eqs. (A.4) and (A.5) are also satisfied. In this quantitative analysis, the formulation will be presented with respect to a dislocation in lattice 1 of Fig. A.1. A similar analogy can be also established for lattice 2.

$$u_k = A_k g(x + py) \quad (\text{A.3})$$

$$(C_{i1k1} + pC_{i1k2} + pC_{i2k1} + p^2C_{i2k2})A_k = 0 \quad (\text{A.4})$$

$$\det(C_{i1k1} + pC_{i1k2} + pC_{i2k1} + p^2C_{i2k2}) = 0 \quad (\text{A.5})$$

For a dislocation of Burgers vector  $\mathbf{b}$ , i.e.  $\mathbf{b} = [b_1, b_2, b_3]$ , the general form of the analytical function  $g(x + py)$ , can be expressed as in Eq. (A.6) where the bar notation implies the complex conjugate of the expression it acts upon. Note that the index 'm' varies from 1 to 6 and no summation convention is implied on it.

$$u_k = \frac{1}{2\pi\sqrt{-1}} \sum_{m=1}^6 \left\{ A_{km}^{(1)} D_m \log(x + p_m y) + \bar{A}_{km}^{(1)} \bar{D}_m \log(x - p_m y) \right\} \quad (\text{A.6})$$

In Eq. (A.6), the parameters  $A_{km}^{(1)}$  and  $D_m$  are related to the components of the Burgers vector  $\mathbf{b}$  by Eq. (A.7) which is an expression of the change in displacement component  $u_k$  along a closed path

**Table A.1**  
The base vectors of  $\mathbf{e}_2$  and  $\mathbf{e}_3$  for lattice 1 (incoming slip) and lattice 2 (outgoing slip) in Reaction 1, 2 and 3 scenarios.

	Lattice 1		Lattice 2	
	$\mathbf{e}_2$	$\mathbf{e}_3$	$\mathbf{e}_2$	$\mathbf{e}_3$
Reaction 1	$1/\sqrt{3}[1\ 1\ -1]_1$	$1/\sqrt{2}[-1\ 1\ 0]_1$	$1/\sqrt{3}[1\ 1\ -1]_2$	$1/\sqrt{2}[1\ -1\ 0]_2$
Reaction 2	$1/\sqrt{3}[1\ -1\ 1]_1$	$1/\sqrt{2}[1\ 1\ 0]_1$	$1/\sqrt{3}[-1\ 1\ 1]_2$	$1/\sqrt{2}[1\ 1\ 0]_2$
Reaction 3	$1/\sqrt{3}[1\ -1\ 1]_1$	$1/\sqrt{2}[-1\ 0\ 1]_1$	$1/\sqrt{3}[1\ -1\ 1]_2$	$1/\sqrt{2}[1\ 1\ 0]_2$

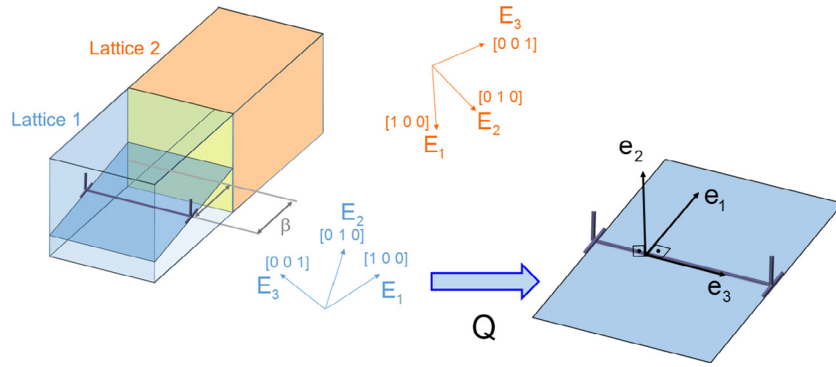


**Fig. A.1.** shows the geometrical configuration of a dislocation posited near the interfacial boundary along the descriptive illustration of coordinate systems and transformation matrix involved.

**Table A.2**

The values of the parameters  $\lambda$ ,  $\mathbf{d}$ ,  $p_1$ ,  $p_2$  and  $p_3$  for the geometrical configurations of incipient slip-grain boundary in Reactions 1, 2 and 3 scenarios. It is to be noted that  $p_1$ ,  $p_2$  and  $p_3$  variables are complex conjugates of  $p_4$ ,  $p_5$  and  $p_6$  respectively in the formulation presented.

	Lattice 1		
	Reaction 1	Reaction 2	Reaction 3
$\lambda$	0	0.078	0.114
$\mathbf{d}$	[0, 0, -9.0435]	[0, 0, 27.1306]	[5.1526, -11.7608, -5.8965]
$p_1$	$-0.5097 + 1.049\sqrt{-1}$	$-0.4783 + 0.8049\sqrt{-1}$	$0.9467 + 1.2601\sqrt{-1}$
$p_2$	$-0.0873 + 0.4941\sqrt{-1}$	$-1.8350 + 1.4745\sqrt{-1}$	$-0.3367 + 0.5475\sqrt{-1}$
$p_3$	$0.5971 + 1.7646\sqrt{-1}$	$0.3323 + 1.6642\sqrt{-1}$	$-0.1117 + 0.8740\sqrt{-1}$

encircling the dislocation line in lattice 1. The superscript (1) stands for lattice 1.

$$\mathbf{b}_k = \sum_{m=1}^6 \left\{ A_{km}^{(1)} D_m + \bar{A}_{km}^{(1)} \bar{D}_m \right\} \quad (\text{A.7})$$

Furthermore, for a pure dislocation, the expression in Eq. (A.8) is to be satisfied to impose the mathematical condition that no line of force distribution acts along the dislocation line:

$$\sum_{m=1}^6 \left\{ (C_{i2k1} + p_m C_{i2k2}) A_{km}^{(1)} D_m + (C_{i2k1} + p_m C_{i2k2}) \bar{A}_{km}^{(1)} \bar{D}_m \right\} = 0 \quad (\text{A.8})$$

Based on the elastic displacement field  $u_k$  in Eq. (A.3), the corresponding stress field is given as:

$$\sigma_{ij} = C_{ijkl} \frac{\partial u_k}{\partial x_l} \quad (\text{A.9})$$

The solution presented above for an homogeneous medium is generalized for a linear elastic medium consisting of multilayered anisotropic plates within the framework of perturbations of the stress and the elastic displacement fields of Eqs. (A.3) and (A.9) in Fourier Space. Following a number of mathematical manipulations, the force acting on a dislocation posited at a distance of  $\beta$  from a welded boundary is expressed as [44,52]:

$$\mathbf{F} = -\text{Re} \left( \frac{\mathbf{b}_k U_{kr} T_{rj} d_j}{4\pi\beta} \right) \quad (\text{A.10})$$

Among the parameters appearing in Eq. (A.10);  $d_j$  satisfies Eq. (A.11)

$$\mathbf{b}_k = b_{kj} d_j \quad (\text{A.11})$$

where  $b_{kj}$  is defined by the expression in Eq. (A.12):

$$b_{kj} = \frac{1}{2} \sqrt{-1} \sum_{m=1}^6 \left\{ A_{km}^{(1)} M_{mj}^{(1)} - \bar{A}_{km}^{(1)} \bar{M}_{mj}^{(1)} \right\} \quad (\text{A.12})$$

The terms  $U_{kr}$  and  $T_{rj}$  in Eq. (A.10) are expressed as:

$$U_{kr} = \left[ \sum_{m=1}^6 \left\{ A_{km}^{(1)} M_{mr}^{(1)} - \bar{A}_{km}^{(2)} \bar{M}_{mr}^{(2)} \right\} \right]^{-1} \quad (\text{A.13})$$

$$T_{rj} = \sum_{m=1}^6 \left\{ \bar{A}_{rm}^{(2)} \bar{M}_{mj}^{(2)} - \bar{A}_{rm}^{(1)} \bar{M}_{mj}^{(1)} \right\} \quad (\text{A.14})$$

where the superscript (2) stands for lattice 2 as shown in Fig. A.1 and  $M_{mi}^{(1)}$  satisfies the following the relation for lattice 1 (and similarly for lattice 2):

$$M_{mi}^{(1)} (C_{i2k1} + p_r C_{i2k2}) A_{kr} = \delta_{mr} \quad (\text{A.15})$$

The resulting values of  $\lambda$ ,  $\mathbf{d}$  and  $(p_1, p_2, p_3)$  triplet involved in the analyses for Reactions 1, 2 and 3 are summarized in Table A.2. It is to be emphasized that  $(p_1, p_2, p_3) = (\bar{p}_4, \bar{p}_5, \bar{p}_6)$  in the nomenclature utilized. The  $\lambda$  value is then utilized in Eqs. (9) and (11) in calculation of the dislocation positions.

## References

- [1] International standard test method for measurement of fatigue crack growth rates, vol. E 647-15. United States: ASTM; 2016.
- [2] Chowdhury P, Sehitoglu H, Rateick R. Recent advances in modeling fatigue cracks at microscale in the presence of high density coherent twin interfaces. *Curr Opin Solid State Mater Sci* 2016;20:140–50.
- [3] Dao M, Lu L, Asaro RJ, De Hosson JTM, Ma E. Toward a quantitative understanding of mechanical behavior of nanocrystalline metals. *Acta Mater* 2007;55:4041–65.
- [4] Lu L, Shen Y, Chen X, Qian L, Lu K. Ultrahigh strength and high electrical conductivity in copper. *Science* 2004;304:422.
- [5] Xu D, Kwan WL, Chen K, Zhang X, Ozoliņš V, Tu KN. Nanotwin formation in copper thin films by stress/strain relaxation in pulse electrodeposition. *Appl Phys Lett* 2007;91:254105.
- [6] Meyers MA, Mishra A, Benson DJ. Mechanical properties of nanocrystalline materials. *Prog Mater Sci* 2006;51:427–556.
- [7] You ZS, Lu L, Lu K. Tensile behavior of columnar grained Cu with preferentially oriented nanoscale twins. *Acta Mater* 2011;59:6927–37.
- [8] Chowdhury P, Sehitoglu H, Maier HJ, Rateick R. Strength prediction in NiCo alloys – the role of composition and nanotwins. *Int J Plast* 2016;79:237–58.
- [9] Pan QS, Lu QH, Lu L. Fatigue behavior of columnar-grained Cu with preferentially oriented nanoscale twins. *Acta Mater* 2013;61:1383–93.

- [10] Sangid MD, Pataky GJ, Sehitoglu H, Rateick RG, Niendorf T, Maier HJ. Superior fatigue crack growth resistance, irreversibility, and fatigue crack growth–microstructure relationship of nanocrystalline alloys. *Acta Mater* 2011;59:7340–55.
- [11] Kobayashi S, Kamata A, Watanabe T. Roles of grain boundary microstructure in high-cycle fatigue of electrodeposited nanocrystalline Ni–P alloy. *Scripta Mater* 2009;61:1032–5.
- [12] Singh A, Tang L, Dao M, Lu L, Suresh S. Fracture toughness and fatigue crack growth characteristics of nanotwinned copper. *Acta Mater* 2011;59:2437–46.
- [13] Alkan S, Chowdhury P, Sehitoglu H, Rateick RG, Maier HJ. Role of nanotwins on fatigue crack growth resistance – experiments and theory. *Int J Fatigue* 2016;84:28–39.
- [14] Chowdhury PB, Sehitoglu H, Rateick RG, Maier HJ. Modeling fatigue crack growth resistance of nanocrystalline alloys. *Acta Mater* 2013;61:2531–47.
- [15] Ezaz T, Sangid MD, Sehitoglu H. Energy barriers associated with slip–twin interactions. *Phil Mag* 2011;91:1464–88.
- [16] Erb U. Electrodeposited nanocrystals: synthesis, properties and industrial applications. *Nanostruct Mater* 1995;6:533–8.
- [17] Miller KJ. Materials science perspective of metal fatigue resistance. *Mater Sci Technol* 1993;9:453–62.
- [18] Pippan R. The condition for the cyclic plastic deformation of the crack tip: the influence of dislocation obstacles. *Int J Fract* 1992;58:305–18.
- [19] Ranganathan S. On the geometry of coincidence-site lattices. *Acta Crystallogr A* 1966;21:197–9.
- [20] Brandon DG, Ralph B, Ranganathan S, Wald MS. A field ion microscope study of atomic configuration at grain boundaries. *Acta Metall* 1964;12:813–21.
- [21] Lange FF. Mathematical characterization of a general bicrystal. *Acta Metall* 1967;15:311–8.
- [22] Rohrer GS, Saylor DM, Dasher BE, Adams BL, Rollett AD, Wynblatt P. The distribution of internal interfaces in polycrystals. *Zeitschrift für Metallkunde* 2004;95:197–214.
- [23] Tschopp MA, McDowell DL. Asymmetric tilt grain boundary structure and energy in copper and aluminium. *Phil Mag* 2007;87:3871–92.
- [24] Patala S, Mason JK, Schuh CA. Improved representations of misorientation information for grain boundary science and engineering. *Prog Mater Sci* 2012;57:1383–425.
- [25] Kelchner CL, Plimpton SJ, Hamilton JC. Dislocation nucleation and defect structure during surface indentation. *Phys Rev B* 1998;58:11085–8.
- [26] Shen Z, Wagoner RH, Clark WAT. Dislocation and grain boundary interactions in metals. *Acta Metall* 1988;36:3231–42.
- [27] Pestman BJ, De Hosson JTM, Vitek V, Schapink FW. Interaction between lattice dislocations and grain boundaries in f.c.c. and ordered compounds: a computer simulation. *Philos Mag A* 1991;64:951–69.
- [28] Grimmer H, Bollmann W, Warrington DH. Coincidence-site lattices and complete pattern-shift in cubic crystals. *Acta Crystallogr Sect A* 1974;30:197–207.
- [29] Wu XJ, Koul AK, Krausz AS. A transgranular fatigue crack growth model based on restricted slip reversibility. *Metall Trans A* 1993;24:1373.
- [30] Mughrabi H, Wang R, Differt K, Essmann U. Fatigue crack initiation by cyclic slip irreversibilities in high-cycle fatigue. *ASTM* 1983:5.
- [31] Chowdhury P, Sehitoglu H. Mechanisms of fatigue crack growth – a critical digest of theoretical developments. *Fatigue Fract Eng Mater Struct* 2016;39:652–74.
- [32] Chowdhury PB, Sehitoglu H, Rateick RG. Predicting fatigue resistance of nanotwinned materials: Part II – effective threshold stress intensity factor range. *Int J Fatigue* 2014;68:292–301.
- [33] Chowdhury PB, Sehitoglu H, Rateick RG. Predicting fatigue resistance of nanotwinned materials: Part I – role of cyclic slip irreversibility and Peierls stress. *Int J Fatigue* 2014;68:277–91.
- [34] Foiles SM, Hoyt JJ. Computation of grain boundary stiffness and mobility from boundary fluctuations. *Acta Mater* 2006;54:3351–7.
- [35] Nosé S. A unified formulation of the constant temperature molecular dynamics methods. *J Chem Phys* 1984;81:511–9.
- [36] Hoover WG. Canonical dynamics: equilibrium phase-space distributions. *Phys Rev A* 1985;31:1695–7.
- [37] Stroh AN. Dislocations and cracks in anisotropic elasticity. *Phil Mag* 1958;3:625–46.
- [38] Alkan S, Sehitoglu H. Non-Schmid response of Fe3Al: the twin-antitwin slip asymmetry and non-glide shear stress effects. *Acta Mater* 2017;125:550–66.
- [39] Alkan S, Sehitoglu H. Dislocation core effects on slip response of NiTi – a key to understanding shape memory. *Int J Plast* 2017.
- [40] Sangid MD, Ezaz T, Sehitoglu H. Energetics of residual dislocations associated with slip–twin and slip–GBs interactions. *Mater Sci Eng, A* 2012;542:21–30.
- [41] Schoeck G. The generalized Peierls–Nabarro model. *Philos Mag A* 1994;69:1085–95.
- [42] Ohr SM. An electron microscope study of crack tip deformation and its impact on the dislocation theory of fracture. *Mater Sci Eng* 1985;72:1–35.
- [43] Majumdar BS, Burns SJ. Crack tip shielding—an elastic theory of dislocations and dislocation arrays near a sharp crack. *Acta Metall* 1981;29:579–88.
- [44] Gemperlová J. Force on dislocations in anisotropic bicrystals and half-spaces. *Phys Status Solidi B* 1968;30:261–74.
- [45] Alexander S. Visualization and analysis of atomistic simulation data with OVITO—the open visualization tool. *Modell Simul Mater Sci Eng* 2010;18:015012.
- [46] Abuzaid W, Sehitoglu H, Lambros J. Plastic strain localization and fatigue micro-crack formation in Hastelloy X. *Mater Sci Eng, A* 2013;561:507–19.
- [47] Lee TC, Robertson IM, Birnbaum HK. TEM in situ deformation study of the interaction of lattice dislocations with grain boundaries in metals. *Philos Mag A* 1990;62:131–53.
- [48] Randle V. Overview No. 127 The role of the grain boundary plane in cubic polycrystals. *Acta Mater* 1998;46:1459–80.
- [49] Elkajbaji M, Thibault-Desseaux J. Interactions of deformation-induced dislocations with  $\Sigma = 9(122)$  grain boundaries in Si studied by HREM. *Philos Mag A* 1988;58:325–45.
- [50] Lim LC, Raj R. Continuity of slip screw and mixed crystal dislocations across bicrystals of nickel at 573 K. *Acta Metall* 1985;33:1577–83.
- [51] Suzuki H. Segregation of solute atoms to stacking faults. *J Phys Soc Jpn* 1962;17:322–5.
- [52] Saxl I. Line and planar singularities in an anisotropic medium. *Czechoslovak J Phys B* 1969;19:836–40.